

Cite this: *Chem. Sci.*, 2024, 15, 8204

All publication charges for this article have been paid for by the Royal Society of Chemistry

# Alloying Pd with Ru enables electroreduction of nitrate to ammonia with ~100% faradaic efficiency over a wide potential window†

Yue Hu,<sup>ab</sup> Jiawei Liu,<sup>c</sup> Wenyu Luo,<sup>b</sup> Jinfeng Dong,<sup>b</sup> Carmen Lee,<sup>b</sup> Nan Zhang,<sup>d</sup> Mengxin Chen,<sup>b</sup> Yifan Xu,<sup>b</sup> Dongshuang Wu,<sup>b</sup> Mingsheng Zhang,<sup>c</sup> Qiang Zhu,<sup>id c</sup> Erhai Hu,<sup>ib b</sup> Dongsheng Geng,<sup>id \*e</sup> Lixiang Zhong<sup>id \*f</sup> and Qingyu Yan<sup>id \*bc</sup>

Electrocatalytic nitrate ( $\text{NO}_3^-$ ) reduction reaction ( $\text{eNO}_3^-$ RR) to ammonia under ambient conditions is deemed a sustainable route for wastewater treatment and a promising alternative to the Haber–Bosch process. However, there is still a lack of efficient electrocatalysts to achieve high  $\text{NH}_3$  production performance at wastewater-relevant low  $\text{NO}_3^-$  concentrations. Herein, we report a  $\text{Pd}_{74}\text{Ru}_{26}$  bimetallic nanocrystal (NC) electrocatalyst capable of exhibiting an average  $\text{NH}_3$  FE of ~100% over a wide potential window from 0.1 to  $-0.3$  V (vs. reversible hydrogen electrode, RHE) at a low  $\text{NO}_3^-$  concentration of 32.3 mM. The average  $\text{NH}_3$  yield rate at  $-0.3$  V can reach  $16.20 \text{ mg h}^{-1} \text{ cm}^{-2}$ . Meanwhile,  $\text{Pd}_{74}\text{Ru}_{26}$  also demonstrates excellent electrocatalytic stability for over 110 h. Experimental investigations and density functional theory (DFT) calculations suggest that the electronic structure modulation between Pd and Ru favors the optimization of  $\text{NO}_3^-$  transport with respect to single components. Along the  $^*\text{NO}_3$  reduction pathway, the synergy between Pd and Ru can also lower the energy barrier of the rate-determining steps (RDSs) on Ru and Pd, which are the protonation of  $^*\text{NO}_2$  and  $^*\text{NO}$ , respectively. Finally, this unique alloying design achieves a high-level dynamic equilibrium of adsorption and coupling between  $^*\text{H}$  and various nitrogen intermediates during  $\text{eNO}_3^-$ RR.

Received 24th January 2024  
Accepted 3rd April 2024

DOI: 10.1039/d4sc00558a

rsc.li/chemical-science

## 1. Introduction

Ammonia ( $\text{NH}_3$ ) not only is a key industrial feedstock for the manufacture of chemicals such as fertilizers,<sup>1</sup> but is also deemed a promising green energy carrier due to its high energy density ( $4.3 \text{ kWh kg}^{-1}$ ), zero carbon emission, and easy liquefaction.<sup>2</sup> For a century, industrial  $\text{NH}_3$  has been mainly produced by the energy- and carbon-intensive Haber–Bosch process.<sup>3</sup> This process consumes about 5.5 EJ of energy ( $\approx 38 \text{ GJ}/t_{\text{NH}_3}$ ) per year and emits over 450 million metric tons of carbon dioxide ( $\approx 2.9 t_{\text{CO}_2}/t_{\text{NH}_3}$ ).<sup>4,5</sup>

Electrocatalytic nitrogen ( $\text{N}_2$ ) reduction reaction ( $\text{eNRR}$ ) and  $\text{eNO}_3^-$ RR using water as a proton source have been explored as appealing alternatives.<sup>6–13</sup> They hold promise for green  $\text{NH}_3$  production due to ambient operating conditions and compatibility with intermittent renewable electricity. Among them,  $\text{eNRR}$  is hindered by the high dissociation energy ( $941 \text{ kJ mol}^{-1}$ ) of the  $\text{N}\equiv\text{N}$  bond and poor solubility ( $6.8 \times 10^{-4} \text{ M}$  in water) of  $\text{N}_2$  in aqueous electrolytes.<sup>14,15</sup> This leads to  $\text{NH}_3$  production being far below the targets for feasible industrial installations imposed by the US Department of Energy (DOE) (current density  $>300 \text{ mA cm}^{-2}$ , FE  $>90\%$ , and yield rate  $>60 \text{ mg h}^{-1} \text{ cm}^{-2}$ ).<sup>16</sup> Compared to  $\text{N}_2$ , the more reactive  $\text{NO}_3^-$  has a significantly lower dissociation energy ( $204 \text{ kJ mol}^{-1}$  for the  $\text{N}=\text{O}$  bond) and absolute solubility in water.<sup>10</sup> This makes  $\text{NO}_3^-$  a more suitable nitrogen source for electrocatalytic  $\text{NH}_3$  synthesis. In fact,  $\text{eNO}_3^-$ RR has a more positive standard reduction potential ( $E_0 = 0.69 \text{ V}$  vs. RHE, hereafter) than  $\text{eNRR}$  ( $E_0 = 0.093 \text{ V}$ ) in an electrolyte at  $\text{pH} = 14$ , implying more favorable thermodynamic conditions.<sup>17</sup> Although  $\text{NO}_3^-$  is a downstream product of  $\text{NH}_3$  in the industry,<sup>18</sup> the availability of environmental pollutant  $\text{NO}_3^-$  makes  $\text{NH}_3$  production by  $\text{eNO}_3^-$ RR a feasible strategy for “turning waste into wealth”. Excessive nitrogen fixation activities of human beings have led to massive amounts of  $\text{NO}_3^-$  being released into the environment. Therefore, various industrial and agricultural effluents rich in  $\text{NO}_3^-$  can be used as

<sup>a</sup>School of Mathematics and Physics, University of Science and Technology Beijing, Beijing, 100083, China

<sup>b</sup>School of Materials Science and Engineering, Nanyang Technological University, 639798, Singapore. E-mail: AlexYan@ntu.edu.sg

<sup>c</sup>Institute of Materials Research and Engineering, A\*STAR, 138634, Singapore

<sup>d</sup>State Key Laboratory of Applied Organic Chemistry, Frontiers Science Center for Rare Isotopes, College of Chemistry and Chemical Engineering, Lanzhou University, Lanzhou, 730000, China

<sup>e</sup>School of Chemistry and Materials Science, Nanjing University of Information Science & Technology, Nanjing, 210044, China. E-mail: dgeng@nuist.edu.cn

<sup>f</sup>School of Physics, Beijing Institute of Technology, Beijing, 100081, China. E-mail: zhonglx@bit.edu.cn

† Electronic supplementary information (ESI) available. See DOI: <https://doi.org/10.1039/d4sc00558a>

$\text{NO}_3^-$  resources for  $\text{eNO}_3^-$ RR to produce  $\text{NH}_3$ . However, most of the practical effluents have low  $\text{NO}_3^-$  concentrations, ranging from a few to tens of mM only.<sup>19,20</sup> In this case, the bias applied to overcome the reaction kinetics of  $\text{eNO}_3^-$ RR to  $\text{NH}_3$  readily induces the competing hydrogen evolution reaction (HER).<sup>21</sup> Hence, it is challenging to design electrocatalysts that can simultaneously achieve high  $\text{NH}_3$  FE and yield rate at low  $\text{NO}_3^-$  concentrations when driven at low potentials.

$\text{eNO}_3^-$ RR to  $\text{NH}_3$  needs to undergo a complex transfer and coupling of eight electrons and nine protons, involving multiple intermediates in the process.<sup>10</sup> Apart from the competing HER, the catalytic performance is also limited by the mismatch in the kinetics of multiple conversion steps.<sup>22,23</sup> It has been reported that the reaction pathway from  $\text{eNO}_3^-$ RR to  $\text{NH}_3$  can be optimized by tuning the adsorption energies of protons and key reaction intermediates.<sup>17,24–28</sup> According to the Sabatier principle, the interaction strength between catalytic sites and reactive species needs to be moderate.<sup>29</sup> In addition, the generation of  $^*\text{H}$  (where  $^*$  denotes an adsorbed species) needs to be ensured to facilitate the deoxygenation and hydrogenation steps of  $\text{eNO}_3^-$ RR to  $\text{NH}_3$ .<sup>30</sup> Palladium (Pd) and ruthenium (Ru) have good water dissociation ability and high coverage of  $^*\text{H}$  on the surface during  $\text{eNO}_3^-$ RR under neutral or alkaline conditions.<sup>31–34</sup> Although this is kinetically favorable for the competing HER, the Pd(111) facet was found to have the ability to catalyze the conversion of  $\text{NO}_3^-$  into  $\text{NO}_2^-$ ,<sup>35</sup> and Ru was found to exhibit significant activity for  $\text{NO}_2^-$  to  $\text{NH}_3$ .<sup>36</sup> This inspired us to alloy these two metals to tailor the geometry and electronic structure of the catalyst, which promises to optimize the adsorption of reactive species while ensuring the supply of  $^*\text{H}$ .

Herein, PdRu bimetallic NCs with different Pd/Ru molar ratios were synthesized and employed as catalysts for  $\text{NH}_3$  production by  $\text{eNO}_3^-$ RR under alkaline conditions.  $\text{Pd}_{74}\text{Ru}_{26}$  NCs exhibit the best  $\text{NH}_3$  production performance. When operating under the  $\text{NO}_3^-$  concentration (32.3 mM) of typical industrial wastewater, an average  $\text{NH}_3$  FE close to 100% can be obtained over a wide potential window (400 mV, from 0.1 to  $-0.3$  V), with an average  $\text{NH}_3$  yield rate of  $16.20 \text{ mg h}^{-1} \text{ cm}^{-2}$  at  $-0.3$  V. When operating at a  $\text{NO}_3^-$  concentration of 100 mM, the potential window for obtaining  $\sim 100\%$   $\text{NH}_3$  FE can be extended from 0.1 to  $-0.9$  V, and the average  $\text{NH}_3$  yield rate at  $-0.9$  V can reach  $42.98 \text{ mg h}^{-1} \text{ cm}^{-2}$ , approaching the DOE targets. Meanwhile,  $\text{Pd}_{74}\text{Ru}_{26}$  NCs also demonstrate excellent electrocatalytic stability during consecutive electrolysis for over 110 h. Moreover, the concentration of nitrate nitrogen ( $\text{NO}_3^-$ -N,  $451.6 \mu\text{g mL}^{-1}$ ) in a simulated industrial wastewater can be decreased to the drinkable water level after 170 min with a final  $\text{NO}_3^-$ -to- $\text{NH}_3$  conversion efficiency over 90%. Experimental investigations and DFT calculations suggest that the electronic structure modulation between Pd and Ru promotes the transport of  $\text{NO}_3^-$ , as well as the protonation of  $^*\text{NO}_2$  (RDS of Ru) and  $^*\text{NO}$  (RDS of Pd).

## 2. Results and discussion

### 2.1 Synthesis and structural characterization

$\text{Pd}_x\text{Ru}_y$  bimetallic NCs with varying Pd/Ru molar ratios ( $x/y$ ) were synthesized through co-electrodepositing Pd and Ru on

porous carbon fiber paper (CFP) under galvanostatic current (Fig. 1a and Methods). As control samples, Pd and Ru NCs were synthesized by monometallic electrodeposition under the same conditions (Methods). During the electroreduction process,  $\text{CO}_2$  was continuously bubbled to compete with the metals for reduction to control the morphology of  $\text{Pd}_x\text{Ru}_y$  NCs. In the case of the precursor Pd and Ru ions at a ratio of 3 : 1, PdRu NCs formed by electrodeposition without  $\text{CO}_2$  bubbling tend to aggregate into bulks (ESI Fig. S1†). The bubbling of  $\text{CO}_2$  broke the PdRu NCs into well-dispersed spherical particles with diameters of around 50 nm (Fig. 1b). From the transmission electron microscopy (TEM) images at higher magnification (Fig. 1c), the PdRu NCs are loosely clustered.

The crystal structures of the Ru, Pd and  $\text{Pd}_x\text{Ru}_y$  NCs were further examined by X-ray diffraction (XRD), high-resolution TEM (HRTEM), and energy-dispersive spectroscopy (EDS). The XRD pattern of Ru NCs (Fig. 1d) displays five broad diffraction peaks in the range of  $35$  to  $75^\circ$ , which can be ascribed to hexagonal close-packed (hcp) Ru (PDF#06-0663). The TEM image (ESI Fig. S2a†) shows that the Ru NCs are highly agglomerated with each crystal size of about 5 nm. The observed lattice spacing of 0.214 nm can match the (002) crystal plane of hcp Ru (ESI Fig. S2b†). The corresponding fast Fourier-transform (FFT) pattern along the  $[0110]$  zone axis (ESI Fig. S2c†) further confirmed the hcp phase of Ru NCs. The three sharp diffraction peaks in the XRD pattern of Pd NCs (Fig. 1d) can be well indexed to the (111), (200) and (220) crystal planes of face-centered cubic (fcc) Pd (PDF#89-4897). The TEM image (ESI Fig. S3a†) shows that Pd NCs show a large diameter of  $\sim 200$  nm. A lattice spacing of 0.228 nm was observed in the HRTEM image (ESI Fig. S3b†), which corresponds to the (111) crystal plane of fcc Pd. In the XRD patterns of  $\text{Pd}_x\text{Ru}_y$  NCs (ESI Fig. S4†), the diffraction peaks of fcc Pd shift toward higher angles after introducing more Ru. This is due to Ru having a smaller ionic radius. Partial alloying of Pd with Ru causes the shrinkage of the lattice.<sup>37</sup> In addition, the weak diffraction peak appearing at  $44.6^\circ$  in the XRD patterns (Fig. 1d and ESI Fig. S2†) can be attributed to the (101) crystal plane of hcp Ru, indicating that slight compositional segregation occurred during the alloying process.<sup>38</sup> The shift of this peak to a higher angle is possibly due to the inherent compressive strain derived from lattice mismatch between the fcc  $\text{Pd}_x\text{Ru}_y$  and hcp Ru.<sup>39</sup> The formation mechanism of fcc  $\text{Pd}_x\text{Ru}_y$  NCs can be inferred as  $\text{Pd}^{2+}$  ions with a high standard electrode potential ( $+0.915 \text{ V}$  versus standard hydrogen electrode, vs. SHE)<sup>40</sup> are preferentially reduced to fcc Pd during the electrodeposition process, and then serve as templates for the growth of Pd and Ru.<sup>41,42</sup> The HRTEM image (Fig. 1e) of  $\text{Pd}_{74}\text{Ru}_{26}$  NCs displays a lattice spacing of 0.224 nm, which is between the fcc Ru(111) interplanar spacing (0.221 nm) and the fcc Pd(111) interplanar spacing (0.228 nm). This is consistent with the XRD results. Moreover, the corresponding FFT pattern (inset of Fig. 1e) along the  $[011]$  zone axis exhibits bright diffraction points indexed to the (111) and (200) crystal planes of fcc  $\text{Pd}_{74}\text{Ru}_{26}$ . The TEM-EDS elemental mapping images (Fig. 1f and S5a†) and the corresponding elemental line scan (Fig. 1g), as well as scanning TEM-EDS elemental mapping images (ESI Fig. S6†) reveal an even distribution of Pd and Ru in



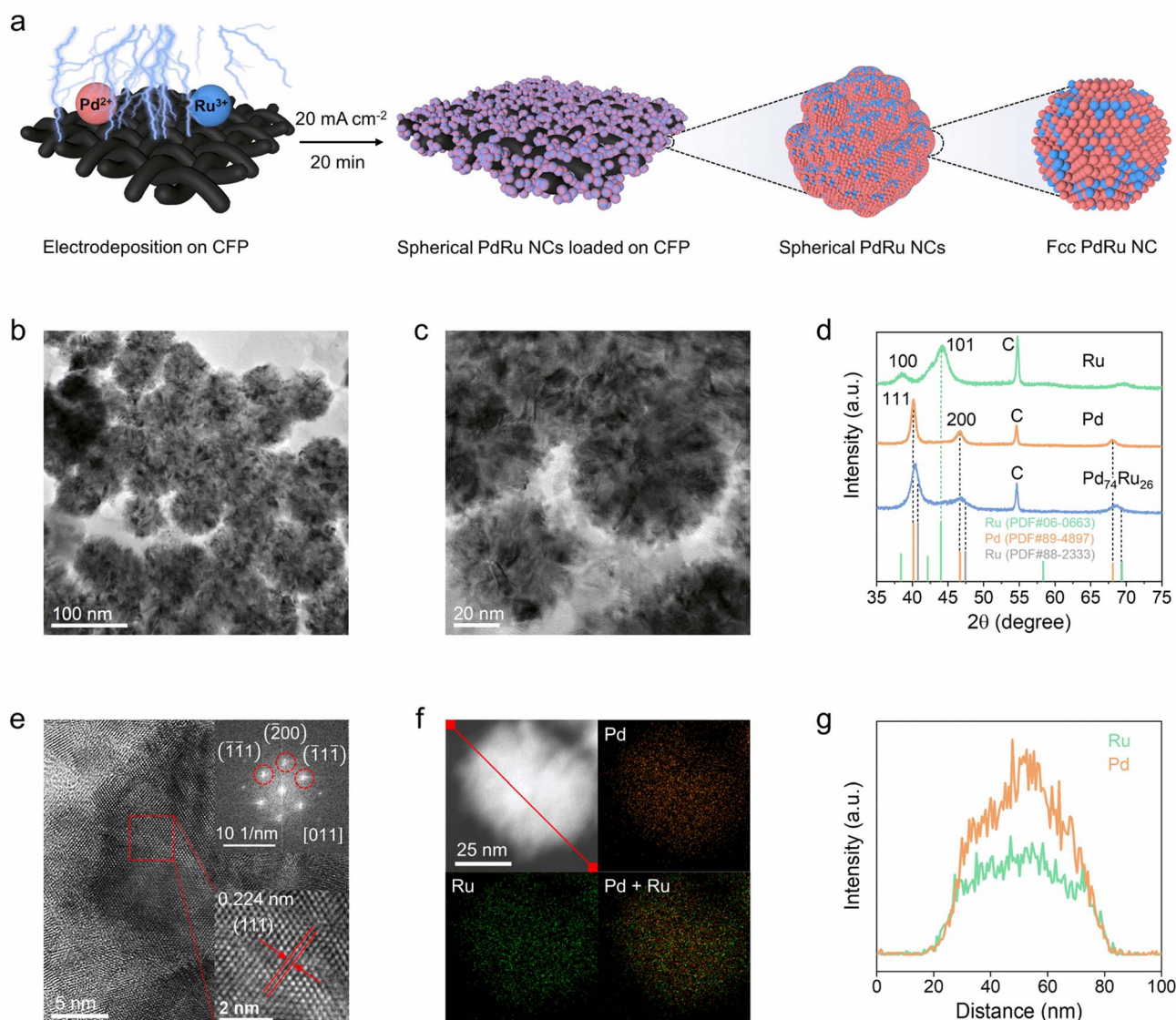


Fig. 1 Synthesis and structural characterization of Pd<sub>74</sub>Ru<sub>26</sub> NCs. (a) Schematic diagram of the synthesis process. (b) and (c) TEM images at different magnifications. (d) XRD patterns of Ru, Pd and Pd<sub>74</sub>Ru<sub>26</sub>. (e) HRTEM image and the corresponding FFT pattern (inset) of the selected area with the red dashed square. (f) TEM-EDS elemental mapping images and (g) corresponding elemental line scan of Pd and Ru.

Pd<sub>74</sub>Ru<sub>26</sub> NCs. Likewise, a uniform distribution of Pd and Ru atoms in both Pd<sub>90</sub>Ru<sub>10</sub> and Pd<sub>57</sub>Ru<sub>43</sub> NCs was also observed (ESI Fig. S7a and S8a<sup>†</sup>). The Pd : Ru atomic ratio of Pd<sub>x</sub>Ru<sub>y</sub> NCs was determined from the EDS spectra as shown in ESI Fig. S5b, Fig. S7b and Fig. S8b.<sup>†</sup> The atomic ratios of Pd and Ru in Pd<sub>x</sub>Ru<sub>y</sub> bimetallic NCs were also determined by inductively coupled plasma optical emission spectroscopy (ICP-OES), and Pd : Cu atomic ratios similar to the EDS results were obtained (ESI Table S1<sup>†</sup>).

The electronic properties of Pd<sub>74</sub>Ru<sub>26</sub> NCs were investigated by X-ray photoelectron spectroscopy (XPS). The XPS survey spectra (ESI Fig. S9<sup>†</sup>) show the existence of obvious Pd 3d, Ru 3p and Ru 3d peaks. The calculated surface Pd/Ru atomic ratio is 74.18 : 25.82 (ESI Table S2<sup>†</sup>) from XPS data, which is also close to the EDS result (ESI Fig. S5b<sup>†</sup>). The Pd<sup>2+</sup> 3d peaks and Ru<sup>4+</sup> 3p

peaks in the deconvoluted Pd 3d XPS spectra (Fig. 2a) and Ru 3p XPS spectra (Fig. 2b), respectively, are due to the partial oxidation of the Pd<sub>74</sub>Ru<sub>26</sub>, Pd and Ru surfaces. In the deconvoluted Pd 3d XPS spectrum of Pd<sub>74</sub>Ru<sub>26</sub> (upper region in Fig. 2a), the peaks located at 335.34 eV and 340.60 eV can be attributed to Pd<sup>0</sup> 3d<sub>5/2</sub> and Pd<sup>0</sup> 3d<sub>3/2</sub>, respectively. Notably, the Pd<sup>0</sup> 3d peaks undergo a negative shift by around 0.29 eV compared with that of Pd (lower region in Fig. 2a), indicating a redistribution of the electrons between Pd and Ru after their alloying. From the deconvoluted Ru 3p XPS spectrum of Pd<sub>74</sub>Ru<sub>26</sub> (upper region in Fig. 2b), the peaks of Ru<sup>0</sup> 3p<sub>3/2</sub> (462.56 eV) and Ru<sup>0</sup> 3p<sub>1/2</sub> (485.24 eV) positively shift by about 0.21 eV compared with that of Ru (lower region in Fig. 2b). Also, a ~0.27 eV positive shift of Ru<sup>0</sup> 3d<sub>5/2</sub> after alloying can be observed in the high-resolution Ru 3d XPS spectra (Fig. 2c), aligning with the C 1s peaks (284.8 eV).



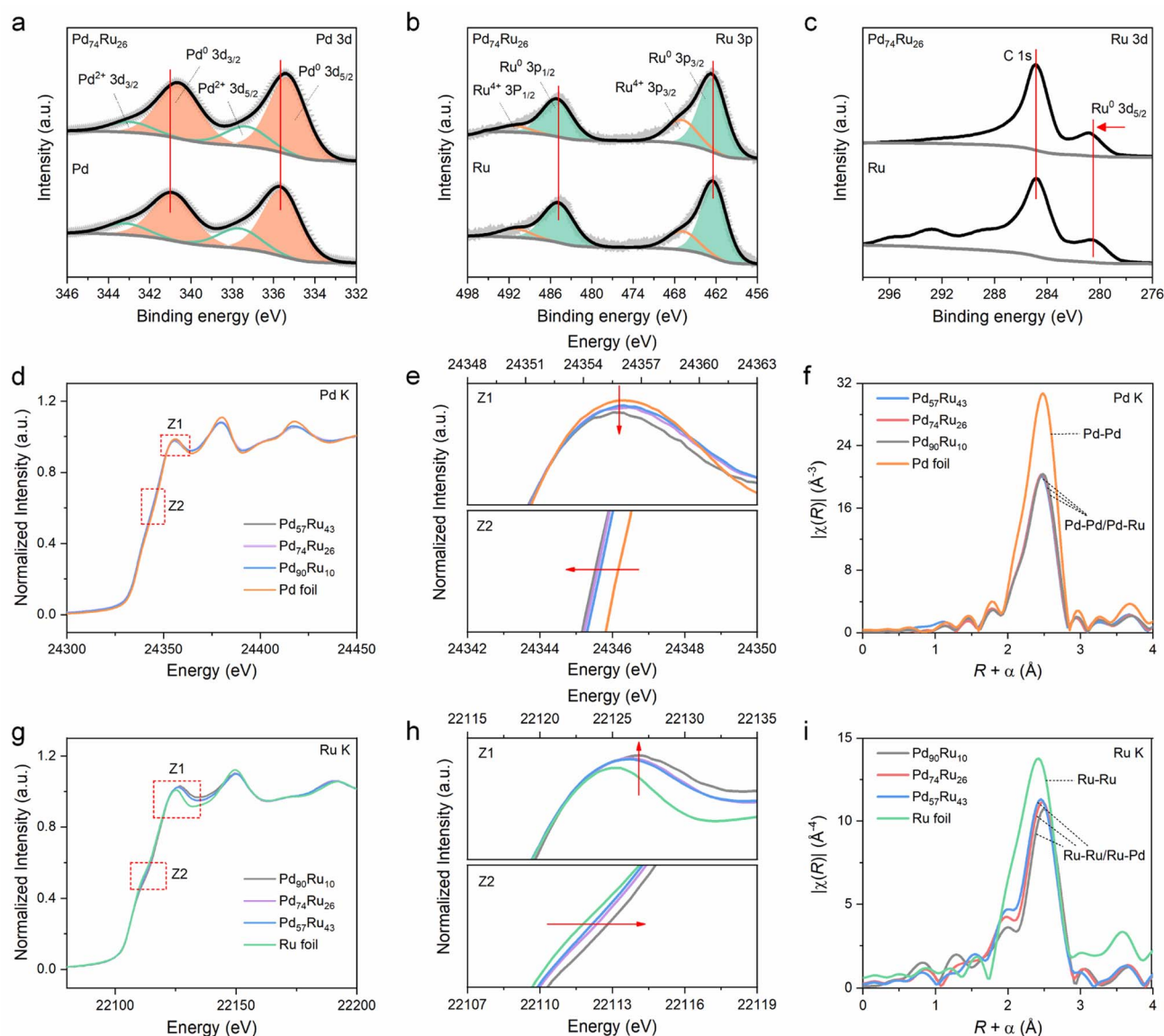


**Fig. 2** Analysis of the electronic properties of  $\text{Pd}_x\text{Ru}_y$  NCs. (a) The deconvoluted Pd 3d XPS spectra of  $\text{Pd}_{74}\text{Ru}_{26}$  and Pd. (b) The deconvoluted Ru 3p XPS spectra of  $\text{Pd}_{74}\text{Ru}_{26}$  and Ru. (c) Ru 3d XPS spectra of  $\text{Pd}_{74}\text{Ru}_{26}$  and Ru. (d) Normalized Pd K-edge XANES spectra of  $\text{Pd}_x\text{Ru}_y$  and Pd foil. (e) Magnified displays of the Z1 and Z2 regions in (d). (f) FT EXAFS spectra of  $\text{Pd}_x\text{Ru}_y$  and Pd foil. (g) Normalized Ru K-edge XANES spectra of  $\text{Pd}_x\text{Ru}_y$  and Ru foil. (h) Magnified displays of the Z1 and Z2 regions in (g). (i) FT EXAFS spectra of  $\text{Pd}_x\text{Ru}_y$  and Ru foil.

These results demonstrate an obvious electron transfer from Ru to Pd in the  $\text{Pd}_{74}\text{Ru}_{26}$  NCs, which will affect the d-band centers and thus the adsorption energies of reactive species.<sup>25,43</sup>

X-ray absorption fine structure spectroscopy (XAFS) was further performed to reveal the electronic interactions and local coordination of Pd and Ru in  $\text{Pd}_x\text{Ru}_y$  NCs. The normalized Pd K-edge X-ray absorption near-edge structure (XANES) spectra (Fig. 2d) show that the absorption near-edge position of  $\text{Pd}_x\text{Ru}_y$  NCs is very close to that of the Pd foil reference. This indicates that Pd exists in a metallic state in  $\text{Pd}_x\text{Ru}_y$  NCs. Zooming in on the Z1 and Z2 regions of Pd K-edge XANES spectra (Fig. 2e), it can be seen that the white line intensity and absorption edge energy gradually decrease with the increase of Ru ratio. This means Ru can induce electron enrichment on Pd in  $\text{Pd}_x\text{Ru}_y$ .

Fig. 2f shows that the Fourier transformed (FT) extended X-ray absorption fine structure (EXAFS) spectra at the Pd K-edge of  $\text{Pd}_x\text{Ru}_y$  are similar to that of Pd foil, but with a negative shift for the main peak as the Ru ratio increases. This indicates that Ru atoms are dissolved into the Pd lattice and coordinate with Pd atoms to form Pd–Ru bonds, which affects the average distance of Pd–Pd bonds. To further know the coordination structure of  $\text{Pd}_x\text{Ru}_y$  NCs and supplement the FT-EXAFS analysis, we fitted the FT-EXAFS curves based on the fcc configuration model (ESI Fig. S10†). The curve fitting results (ESI Table S3†) reveal the scattering path of Pd–Pd/Ru in  $\text{Pd}_x\text{Ru}_y$  with a coordination number of around 10, which is evidently lower than that (12) of Pd foil. Besides, in comparison with Pd foil, the fcc  $\text{Pd}_x\text{Ru}_y$  NCs exhibit a shorter interatomic distance ( $R_{\text{Pd-Pd/Ru}}$ ), which

decreases as the Ru ratio increases. Fig. 2g shows a similar normalized Ru K-edge XANES spectra of the  $\text{Pd}_x\text{Ru}_y$  NCs and Ru foil reference, also indicating that Ru exists in a metallic state in  $\text{Pd}_x\text{Ru}_y$  NCs. Compared with Pd K-edge XANES spectra, the magnified displays of the Z1 and Z2 regions in Ru K-edge XANES spectra signify that the white line intensity and absorption edge energy increase with the Pd ratio in  $\text{Pd}_x\text{Ru}_y$ . This proves that the electron enrichment of Pd in  $\text{Pd}_x\text{Ru}_y$  is due to the electron transfer from Ru to Pd, which is in line with XPS results. From the FT EXAFS spectra at the Ru K-edge (Fig. 2i), the position of the main peak attributed to the Ru-M (M = Ru/Pd) scattering path shifts positively with increasing Pd ratio in  $\text{Pd}_x\text{Ru}_y$ . This further demonstrates the solid solution characteristics of Ru and Pd in  $\text{Pd}_x\text{Ru}_y$ . The impact of electron redistribution within Pd and Ru in  $\text{Pd}_{74}\text{Ru}_{26}$  on water dissociation and the adsorption of reactive species will be further discussed in the mechanistic analysis section.

## 2.2 Electrochemical activity and kinetics analysis

The electrochemically active surface areas (ECSAs) of the Pd, Ru and  $\text{Pd}_{74}\text{Ru}_{26}$  NCs were evaluated by measuring the electric double layer capacitance ( $C_{\text{dl}}$ ). On the basis of the cyclic voltammetry (CV) curves obtained at different scan rates (ESI Fig. S11†), the  $C_{\text{dl}}$  for Pd, Ru and  $\text{Pd}_{74}\text{Ru}_{26}$  NCs was calculated to be 99.82, 84.68 and 110.08  $\text{mF cm}^{-2}$ , respectively (Fig. 3a). This indicates that the spherical  $\text{Pd}_{74}\text{Ru}_{26}$  NCs expose more active

sites than highly agglomerated Ru NCs and large-diameter Pd NCs. Linear sweep voltammetry (LSV) tests were performed to investigate the reaction activity and kinetics of Pd, Ru and  $\text{Pd}_x\text{Ru}_y$  NCs for  $\text{eNO}_3^-$ RR. As shown in Fig. 3b,  $\text{Pd}_x\text{Ru}_y$  exhibit more positive onset potentials and larger current responses for  $\text{eNO}_3^-$ RR compared to Pd and Ru. This suggests that the alloying of Pd with Ru can effectively enhance  $\text{NO}_3^-$  adsorption/activation and improve the catalytic activity for  $\text{eNO}_3^-$ RR. The highest current density during the potential variation implies that  $\text{Pd}_{74}\text{Ru}_{26}$  is the best  $\text{eNO}_3^-$ RR catalyst among  $\text{Pd}_x\text{Ru}_y$ . This may be due to the fact that the electronic interaction of Pd and Ru in  $\text{Pd}_x\text{Ru}_y$  is affected by the composition ratio, and this electronic modulation is directly related to its adsorption of reactants. According to the Sabatier principle,<sup>29</sup> catalysts with moderate adsorption energy are provided with the best catalytic activity. Therefore, by optimizing the component ratio in  $\text{Pd}_x\text{Ru}_y$ ,  $\text{Pd}_{74}\text{Ru}_{26}$  can achieve superior  $\text{eNO}_3^-$ RR activity. Tafel slopes were derived from the LSV curves (Fig. 3c) to evaluate the electron transfer kinetics of Pd, Ru and  $\text{Pd}_x\text{Ru}_y$  NCs during  $\text{eNO}_3^-$ RR.  $\text{Pd}_{74}\text{Ru}_{26}$  exhibits a Tafel slope of  $188.02 \text{ mV dec}^{-1}$ , which is lower than that of Pd ( $223.19 \text{ mV dec}^{-1}$ ) and Ru ( $205.09 \text{ mV dec}^{-1}$ ). This indicates that alloying Pd and Ru in an optimized ratio can promote the electron transfer for  $\text{eNO}_3^-$ RR. This is supported by the smaller charge-transfer resistance ( $R_{\text{ct}}$ ) of  $\text{Pd}_{74}\text{Ru}_{26}$  ( $0.27 \Omega$ ) compared to Ru ( $0.45 \Omega$ ) and Pd ( $1.01 \Omega$ ) during  $\text{eNO}_3^-$ RR, as known from electrochemical impedance spectra (EIS, Fig. 3d).

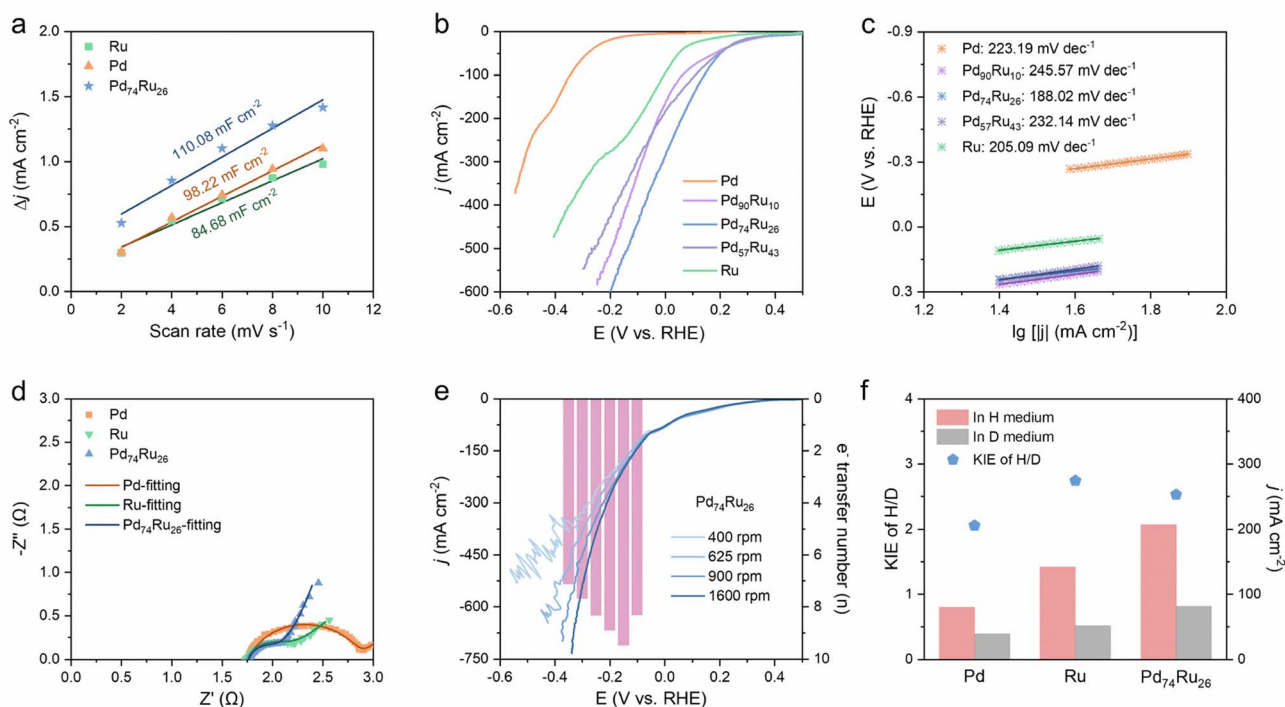


**Fig. 3** Electrochemical activity and kinetics analysis of Pd, Ru and  $\text{Pd}_x\text{Ru}_y$  NCs. (a) Calculated  $C_{\text{dl}}$  for Pd, Ru and  $\text{Pd}_{74}\text{Ru}_{26}$  NCs. (b) LSV curves (80%  $iR$  corrected) of Pd, Ru and  $\text{Pd}_x\text{Ru}_y$  NCs in 1 M KOH with 100 mM  $\text{NO}_3^-$ . (c) Corresponding Tafel slopes of the LSV curves. (d) EIS of Pd at  $-0.3 \text{ V}$ , Ru at  $0.1 \text{ V}$  and  $\text{Pd}_{74}\text{Ru}_{26}$  at  $0.2 \text{ V}$  during  $\text{eNO}_3^-$ RR. (e) LSV curves (80%  $iR$  corrected) at different rotation rates in 1 M KOH with 100 mM  $\text{NO}_3^-$ , and corresponding electron transfer numbers at different potentials for  $\text{Pd}_{74}\text{Ru}_{26}$  NCs. (f)  $\text{KIE}_{(\text{H/D})}$  values of Pd, Ru and  $\text{Pd}_{74}\text{Ru}_{26}$  NCs estimated using the ratio of current density in a purely protic medium and a purely deuterium medium.



To examine the  $\text{NO}_3^-$  to  $\text{NH}_3$  conversion on the catalysts, the number of transferred electrons ( $n$ ) on Pd (ESI Fig. S12a†), Ru (ESI Fig. S12b†) and  $\text{Pd}_{74}\text{Ru}_{26}$  (Fig. 3e) during  $\text{eNO}_3^-$ RR was estimated from the slopes of the Koutecký-Levich (K-L) plots (ESI Fig. S13†). For Pd, the  $n$  values from  $-0.4$  to  $-0.55$  V are close to 3, indicating that Pd is more prone to the 2-electron transfer reaction from  $\text{NO}_3^-$  to  $\text{NO}_2^-$ . Unlike Pd, the  $n$  values of Ru in the potential interval of  $-0.1$  to  $-0.35$  V are  $>5$ . This signifies that the steps involving multi-electron (compared to 2-electron) transfer in  $\text{eNO}_3^-$ RR can occur on Ru, which is conducive to the generation of the final product  $\text{NH}_3$ . After alloying Pd and Ru to  $\text{Pd}_{74}\text{Ru}_{26}$ , direct 8-electron transfer processes are seen over the potential range between  $-0.1$  and  $-0.35$  V. This suggests that the direct reduction of  $\text{NO}_3^-$  to  $\text{NH}_3$  occurs readily over  $\text{Pd}_{74}\text{Ru}_{26}$ . Additionally, a quasi-first-order reaction kinetics relationship between current density and  $\text{NO}_3^-$  concentration on  $\text{Pd}_{74}\text{Ru}_{26}$  at  $-0.1$  V is obtained (ESI Fig. S14†). This indicates that  $\text{eNO}_3^-$ RR on  $\text{Pd}_{74}\text{Ru}_{26}$  driven by this potential is only related to the adsorption of  $\text{NO}_3^-$ , and is not subject to the kinetic constraints of the intermediate reaction steps.

To explore the  $^*\text{H}$  usage capability of the catalysts during  $\text{eNO}_3^-$ RR, the proton transfer rate was evaluated through the kinetic isotope effect (KIE) of H/D ( $\text{KIE}_{\text{H/D}}$ ) (ESI Fig. S15†).<sup>28,30</sup> As shown in Fig. 3f, the  $\text{KIE}_{\text{H/D}}$  values of Pd at  $-0.3$  V, Ru at 0 V and  $\text{Pd}_{74}\text{Ru}_{26}$  at 0 V are 2.06, 2.74 and 2.52, respectively. They all refer to the primary kinetic isotope effect, suggesting that the rate-determining step (RDS) of  $\text{eNO}_3^-$ RR involves breaking the H-OH bond of  $\text{H}_2\text{O}$  and coupling  $^*\text{H}$  with nitrogen intermediates.<sup>27</sup> The lowest  $\text{KIE}_{\text{H/D}}$  value of Pd indicates that it has the optimum water dissociation and  $^*\text{H}$  consumption rates, but is driven at a more negative potential. At 0 V, the lower  $\text{KIE}_{\text{H/D}}$  value of  $\text{Pd}_{74}\text{Ru}_{26}$  compared to Ru demonstrates that the  $^*\text{H}$  transfer kinetics associated with the RDS of  $\text{eNO}_3^-$ RR is improved. Combined with the analysis of K-L plots, it can be deduced that alloying Pd with Ru in a reasonable ratio can optimize the adsorption/coupling of protons and nitrogen intermediates to a high level of dynamic equilibrium.

### 2.3 Performance of $\text{eNO}_3^-$ RR

The performance of  $\text{eNO}_3^-$ RR to  $\text{NH}_3$  on Pd, Ru and  $\text{Pd}_{74}\text{Ru}_{26}$  NCs was first evaluated at an industrial wastewater-relevant  $\text{NO}_3^-$  concentration of 32.3 mM (2000 ppm)<sup>44,45</sup> under ambient conditions using a standard three-electrode H-type cell (Methods). LSV curves of Pd, Ru and  $\text{Pd}_{74}\text{Ru}_{26}$  NCs (Fig. 4a) preliminarily show that they all have  $\text{eNO}_3^-$ RR activity, as reflected by the positively shifted onset potentials and increased current densities after adding  $\text{NO}_3^-$ . The lowest onset potential of 0.3 V and the maximum increase in current density indicate an optimized  $\text{eNO}_3^-$ RR activity of  $\text{Pd}_{74}\text{Ru}_{26}$  NCs as compared to the other two samples. To further determine the contribution of  $\text{eNO}_3^-$ RR activity to  $\text{NH}_3$  production, we performed 1 h potentiostatic  $\text{eNO}_3^-$ RR on Pd, Ru and  $\text{Pd}_{74}\text{Ru}_{26}$  at different applied potentials, respectively (ESI Fig. S16†). The average FE (Fig. 4b) of the main products  $\text{NO}_2^-$  and  $\text{NH}_3$  was then calculated by detecting the remaining  $\text{NO}_3^-$  as well as  $\text{NO}_2^-$  and  $\text{NH}_3$  in the

post-reaction electrolyte.  $\text{NO}_x^-$  ( $\text{NO}_3^-$  and  $\text{NO}_2^-$ ) and  $\text{NH}_3$  were quantitatively determined by ultraviolet-visible (UV-vis) spectrophotometry and ion chromatography with calibration curves, respectively (ESI Fig. S17 and S18†). As shown in Fig. 4b, both  $\text{Pd}_{74}\text{Ru}_{26}$  and Ru showed high  $\text{NH}_3$  FE over 98% at a positive applied potential of 0.1 V, while Pd has no  $\text{eNO}_3^-$ RR activity yet. The  $\text{NH}_3$  yield rate of  $\text{Pd}_{74}\text{Ru}_{26}$  is  $4.4 \text{ mg h}^{-1} \text{ cm}^{-2}$ , which is almost 3 times that of Ru (Fig. 4c). Despite the satisfactory  $\text{NH}_3$  FE of  $\text{Pd}_{74}\text{Ru}_{26}$  and Ru, their  $\text{NH}_3$  yield rates are well below the DOE targets of  $>60 \text{ mg h}^{-1} \text{ cm}^{-2}$ .<sup>16</sup> Hence, the  $\text{NH}_3$  production performance of these three catalysts at more negative potentials was further analyzed. Pd exhibits  $\sim 66\%$   $\text{NH}_3$  FE at tested potentials from  $-0.3$  to  $-0.5$  V, all accompanied by a considerable  $\text{NO}_2^-$  FE of  $\sim 20\%$  (Fig. 4b). This suggests that Pd has good  $\text{NO}_3^-$  to  $\text{NO}_2^-$  conversion ability, but the kinetics of  $^*\text{NO}_2^-$  hydrogenation to  $^*\text{NH}_3$  is weak, leading to an accumulation of  $\text{NO}_2^-$ . The average  $\text{NH}_3$  FE of Ru decreases from 98.2% at 0.1 V to 60.5% at  $-0.5$  V as the potential shifts negatively. At  $-0.5$  V, the negligible  $\text{NO}_2^-$  FE and the observed substantial bubble generation during the reaction indicate that the main competition for the reduction of  $\text{NO}_3^-$  to  $\text{NH}_3$  on Ru is the HER. For  $\text{Pd}_{74}\text{Ru}_{26}$ , an average  $\text{NH}_3$  FE close to 100% is obtained over a wide potential window from 0.1 to  $-0.3$  V, signifying a near-complete conversion of participating  $\text{NO}_3^-$  to  $\text{NH}_3$  during the 1 h  $\text{eNO}_3^-$ RR process. At  $-0.3$  V, the average  $\text{NH}_3$  yield rate and  $j_{\text{NH}_3}$  of  $\text{Pd}_{74}\text{Ru}_{26}$  reach respectively  $16.2 \text{ mg h}^{-1} \text{ cm}^{-2}$  and  $208.0 \text{ mA cm}^{-2}$ , which are 7.2 and 9.1 times higher than those of Pd (Fig. 4c and d). Although Ru shows a relatively high  $\text{NH}_3$  FE of 89.7% at  $-0.3$  V, the average  $\text{NH}_3$  yield rate and  $j_{\text{NH}_3}$  are only  $11.8 \text{ mg h}^{-1} \text{ cm}^{-2}$  and  $152.4 \text{ mA cm}^{-2}$  (Fig. 4c and d). The difference in  $\text{NH}_3$  production performance between Ru and  $\text{Pd}_{74}\text{Ru}_{26}$  becomes increasingly prominent with the negative shift of potential. At  $-0.5$  V, the average  $\text{NH}_3$  FE,  $\text{NH}_3$  yield rate and  $j_{\text{NH}_3}$  of  $\text{Pd}_{74}\text{Ru}_{26}$  are respectively 91.6%,  $20.6 \text{ mg h}^{-1} \text{ cm}^{-2}$  and  $261.0 \text{ mA cm}^{-2}$ , which are about 1.5, 1.7 and 1.7 times those of Ru. These results demonstrate a good synergistic catalytic behavior of Pd and Ru in  $\text{Pd}_{74}\text{Ru}_{26}$  for  $\text{NH}_3$  production by  $\text{eNO}_3^-$ RR. To unveil the intrinsic activity of the catalysts, we normalized the current density by the ECSA (ESI Table S4†). Although  $\text{Pd}_{74}\text{Ru}_{26}$  and Ru present similar ECSA-normalized total current density curves (ESI Fig. S19a†),  $\text{Pd}_{74}\text{Ru}_{26}$  shows the largest ECSA-normalized  $j_{\text{NH}_3}$  at each potential (ESI Fig. S19b†). This indicates that alloying Pd and Ru to  $\text{Pd}_{74}\text{Ru}_{26}$  synergistically promotes the intrinsic activity of  $\text{eNO}_3^-$ RR to  $\text{NH}_3$ .

N isotope labeled  $\text{eNO}_3^-$ RR experiments and  $^1\text{H}$  nuclear magnetic resonance (NMR) tests were performed to assess the origin of the detected ammonia nitrogen ( $\text{NH}_3\text{-N}$ ) (Fig. 4e). After running  $\text{eNO}_3^-$ RR on  $\text{Pd}_{74}\text{Ru}_{26}$  in  $\text{NO}_3^-$ -free electrolyte (ESI Fig. S20a†),  $\text{NH}_3$  was barely detected in the post-reaction electrolyte (ESI Fig. S20b†). As expected, there was no  $\text{NH}_4^+$  signal in the  $^1\text{H}$  NMR spectrum. After running  $\text{eNO}_3^-$ RR on  $\text{Pd}_{74}\text{Ru}_{26}$  with  $^{14}\text{NO}_3^-$  and  $^{15}\text{NO}_3^-$  sources, clear characteristic signals corresponding to  $^{14}\text{NH}_4^+$  (triple peaks) and  $^{15}\text{NH}_4^+$  (double peaks) appeared in the  $^1\text{H}$  NMR spectra of the post-reaction electrolytes, respectively. This proves that the product  $\text{NH}_3\text{-N}$  does originate from  $\text{eNO}_3^-$ RR. Afterwards, the  $^{15}\text{NH}_3$



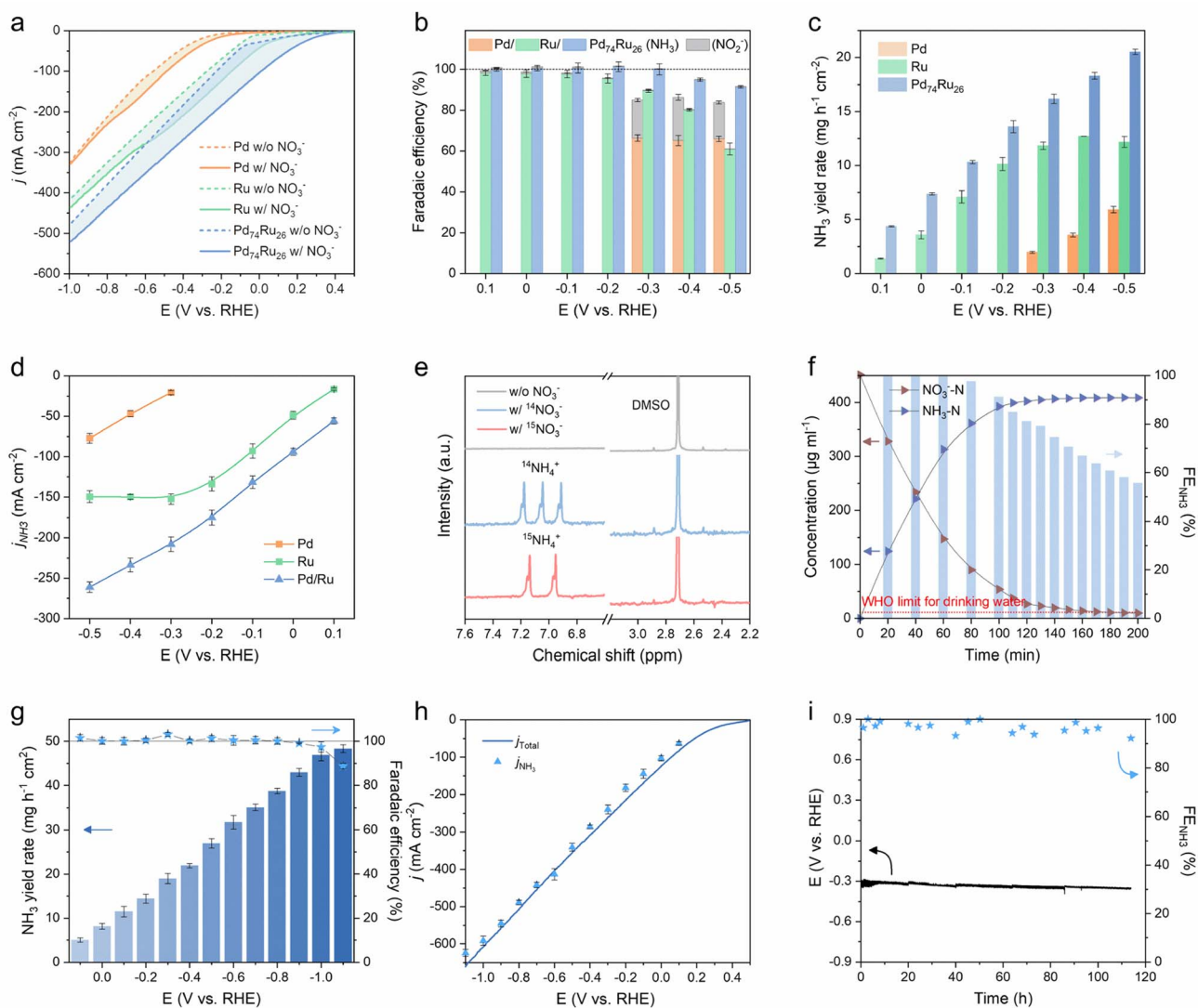


Fig. 4 Performance of eNO<sub>3</sub><sup>-</sup>RR. LSV curves of Pd, Ru and Pd<sub>74</sub>Ru<sub>26</sub> NCs in 1 M KOH with/without 32.3 mM NO<sub>3</sub><sup>-</sup> (a), and the corresponding NH<sub>3</sub> and NO<sub>2</sub><sup>-</sup> FE (b), NH<sub>3</sub> yield rate (c), and *j*<sub>NH<sub>3</sub></sub> (d) in 1 M KOH with 32.3 mM NO<sub>3</sub><sup>-</sup>. (e) <sup>1</sup>H NMR spectra of electrolytes after eNO<sub>3</sub><sup>-</sup>RR without NO<sub>3</sub><sup>-</sup>, with 32.3 mM <sup>14</sup>NO<sub>3</sub><sup>-</sup>, and with 32.3 mM <sup>15</sup>NO<sub>3</sub><sup>-</sup> sources, respectively. (f) Time-dependent concentration of NO<sub>3</sub><sup>-</sup>-N, NH<sub>3</sub>-N, and NO<sub>2</sub><sup>-</sup>-N and corresponding NH<sub>3</sub> FE for eNO<sub>3</sub><sup>-</sup>RR using Pd<sub>74</sub>Ru<sub>26</sub> NCs at -0.3 V in simulated industrial wastewater containing 1 M KOH and 32.3 mM NO<sub>3</sub><sup>-</sup>. NH<sub>3</sub> FE and yield rate (g) as well as *j*<sub>NH<sub>3</sub></sub> and LSV curve (h) of Pd<sub>74</sub>Ru<sub>26</sub> NCs in 1 M KOH with 100 mM NO<sub>3</sub><sup>-</sup>. (i) Long-term CP stability test of Pd<sub>74</sub>Ru<sub>26</sub> NCs at 200 mA cm<sup>-2</sup> in 1 M KOH with 32.3 mM NO<sub>3</sub><sup>-</sup> using an H-type flow cell.

yield rate was quantified by the linear fitting calibration curves obtained from the <sup>1</sup>H NMR peaks. The results agree well with the UV-vis spectrophotometric measurement results, proving the reliability of the ammonia production performance test (ESI Fig. S21†). Additionally, we performed control experiments with a bare CFP electrode to confirm that eNO<sub>3</sub><sup>-</sup>RR principally occurs on Pd<sub>74</sub>Ru<sub>26</sub> (ESI Fig. S22†). Considering the incompletely exposed CFP area in the Pd<sub>74</sub>Ru<sub>26</sub>/CFP electrode and the extremely low NH<sub>3</sub> yield rates of the bare CFP electrode, the impact of CFP on the performance results of Pd<sub>74</sub>Ru<sub>26</sub> is negligible.

To evaluate the NO<sub>3</sub><sup>-</sup> removal capacity of Pd<sub>74</sub>Ru<sub>26</sub> in simulated industrial wastewater, a continuous eNO<sub>3</sub><sup>-</sup>RR was carried out at -0.3 V with a starting NO<sub>3</sub><sup>-</sup> concentration of

32.3 mM (equivalent to 451.6 μg ml<sup>-1</sup> NO<sub>3</sub><sup>-</sup>-N). The conversion of elemental N was tracked by determining the concentrations of NO<sub>3</sub><sup>-</sup>, NO<sub>2</sub><sup>-</sup> and NH<sub>3</sub> in the electrolyte at different times (Fig. 4f). As eNO<sub>3</sub><sup>-</sup>RR proceeded, NO<sub>3</sub><sup>-</sup>-N was gradually reduced to NH<sub>3</sub>-N with a conversion rate of 90.6% at the 200th min (ESI Fig. S23†). No toxic pollutant NO<sub>2</sub><sup>-</sup> was detected in the entire electrolysis process, which prevented the secondary pollution to the environment. After 170 min of electrolysis, the residual NO<sub>3</sub><sup>-</sup>-N (11.26 μg ml<sup>-1</sup>) fell below the acceptable drinking water level (<11.29 μg ml<sup>-1</sup>) stipulated by the World Health Organization (WHO).<sup>46</sup> It should be mentioned that the NH<sub>3</sub> FE was maintained at ~100% until the NO<sub>3</sub><sup>-</sup>-N dropped to 147.4 μg ml<sup>-1</sup> (*i.e.*, 10.5 mM NO<sub>3</sub><sup>-</sup>) after 1 hour.

To explore the potential of Pd<sub>74</sub>Ru<sub>26</sub> for NH<sub>3</sub> production with ~100% FE over a wider NO<sub>3</sub><sup>−</sup> concentration range, we examined its NH<sub>3</sub> production performance at a starting NO<sub>3</sub><sup>−</sup> concentration of 100 mM. As shown in Fig. 4g, the potential window for obtaining ~100% NH<sub>3</sub> FE can be extended from 0.1 to −0.9 V, and the average NH<sub>3</sub> yield rate at −0.9 V can reach 42.98 mg h<sup>−1</sup> cm<sup>−2</sup>, approaching the DOE target of >60 mg h<sup>−1</sup> cm<sup>−2</sup>.<sup>16</sup> The nearly consistent agreement between the average *j*<sub>NH<sub>3</sub></sub> and LSV curves at different potentials in this potential interval further verified the performance of Pd<sub>74</sub>Ru<sub>26</sub> for NH<sub>3</sub> production with full FE (Fig. 4h). The performance of Pd<sub>74</sub>Ru<sub>26</sub> for NH<sub>3</sub> production by eNO<sub>3</sub><sup>−</sup>RR exceeds that of most previously reported electrocatalysts (ESI Fig. S24 and Table S5†).

Long-term stability of a catalyst is crucial for its practical applications. Here, an over 100 h chronopotentiometry (CP) test was conducted in an H-type flow cell to assess the catalytic stability of Pd<sub>74</sub>Ru<sub>26</sub> (Fig. 4i). The potential maintaining a current density of 200 mA cm<sup>−2</sup> was stable around −0.3 V with measured NH<sub>3</sub> FE over 90% at different times. The XRD patterns (ESI Fig. S25†), TEM mapping images (ESI Fig. S26†) and HRTEM image (ESI Fig. S27†) of Pd<sub>74</sub>Ru<sub>26</sub> after the stability test reveal no obvious changes in its morphology and structure. Moreover, the XPS analysis of Pd<sub>74</sub>Ru<sub>26</sub> after a 114 h CP test shows little change in the chemical compositions and oxidation states (ESI Fig. S28 and Table S2†). These results suggest that the structurally stable Pd<sub>74</sub>Ru<sub>26</sub> NCs possess remarkable catalytic stability for eNO<sub>3</sub><sup>−</sup>RR to NH<sub>3</sub>.

## 2.4 Reaction mechanism analysis

Operando Fourier transform infrared spectroscopy (FTIR) tests were performed to detect the reactive species on Pd, Ru and Pd<sub>74</sub>Ru<sub>26</sub> during eNO<sub>3</sub><sup>−</sup>RR from OCP to −1 V, as shown in Fig. 5a–c. Positive and negative infrared bands correspond to consumed and produced species, respectively.<sup>47</sup> At the open circuit potential (OCP), the FTIR spectra of Pd, Ru and Pd<sub>74</sub>Ru<sub>26</sub> have no obvious signals. When the applied potential gradually shifts negatively, some characteristic peaks appear. For Pd, the characteristic peaks located at ~1130 cm<sup>−1</sup>, ~1240 cm<sup>−1</sup>, ~1445 cm<sup>−1</sup>, and ~1625 cm<sup>−1</sup> can be respectively assigned to the N–O bond, the N–O antisymmetric stretching of NO<sub>2</sub><sup>−</sup>, the wagging of −NH<sub>2</sub>, and the bending of H<sub>2</sub>O.<sup>28,37</sup> For Ru and Pd<sub>74</sub>Ru<sub>26</sub>, besides the same characteristic peaks as Pd, characteristic peaks located at ~1345 cm<sup>−1</sup>, ~3380 cm<sup>−1</sup>, and ~3750 cm<sup>−1</sup> can also be observed. They can be attributed to the N–O asymmetric stretching vibration of NO<sub>3</sub><sup>−</sup>, the O–H stretching of H<sub>2</sub>O, and the bending of N–H,<sup>28,37</sup> respectively. Among them, the emergence of −NH<sub>2</sub> wagging and N–H bending confirms the formation of NH<sub>3</sub>. The emergence of the N–O bond and the N–O antisymmetric stretching of NO<sub>2</sub><sup>−</sup> means the formation of key intermediates in the deoxygenation process. The emergence of O–H stretching and H<sub>2</sub>O bending indicates the involvement of H<sub>2</sub>O in the reaction. In the FTIR spectra of Ru and Pd<sub>74</sub>Ru<sub>26</sub>, the peak intensity of the N–O asymmetric stretching vibration of NO<sub>3</sub><sup>−</sup> gradually increases

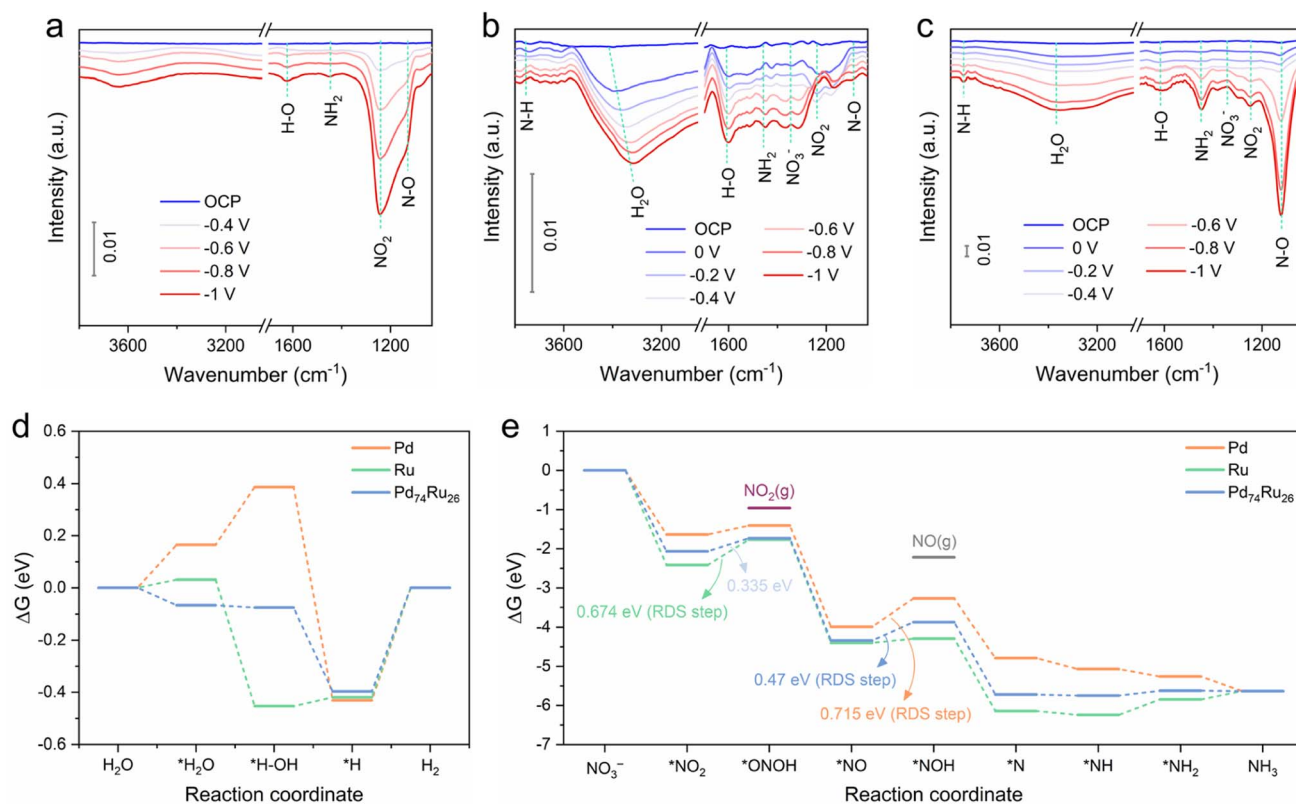


Fig. 5 Operando FTIR spectra collected on Pd (a), Ru (b) and Pd<sub>74</sub>Ru<sub>26</sub> (c) during eNO<sub>3</sub><sup>−</sup>RR from OCP to −1 V. The free energy diagram of each intermediate state during the HER (d) and eNO<sub>3</sub>RR (e) on the three surfaces calculated at 0 V.

with the potential, indicating the consumption of  $\text{NO}_3^-$ . From the FTIR spectra collected on Pd, the most intense peak is the N–O antisymmetric stretching of  $\text{NO}_2^-$ . This indicates the presence of considerable  $\text{NO}_2^-$  on the Pd surface, consistent with experimental observations (Fig. 4b). From the FTIR spectra collected on Ru and  $\text{Pd}_{74}\text{Ru}_{26}$ , the most intense peaks are the  $\text{H}_2\text{O}$  bending and N–O bond, respectively. This indicates that  $\text{eNO}_3^-$ RR occurs more fully on  $\text{Pd}_{74}\text{Ru}_{26}$ , also consistent with experimental observations (Fig. 4b). According to the above results, the volcano-type relationship between  $\text{Pd}_x\text{Ru}_y$  and  $\text{eNO}_3^-$ RR activity can be further explained as follows. For  $\text{Pd}_{90}\text{Ru}_{10}$ , a large amount of Pd may lead to insufficient adsorption of intermediate  $\text{NO}_2$ , thereby inhibiting the subsequent conversion of  $\text{NO}_2$  to  $\text{NH}_3$ . For  $\text{Pd}_{57}\text{Ru}_{43}$ , excess Ru may lead to excessive adsorption of  $\text{H}_2\text{O}$ , which is not conducive to the coupling of protons and nitrogen intermediates. Alloying Pd and Ru to  $\text{Pd}_{74}\text{Ru}_{26}$  can optimize the adsorption/coupling of proton and nitrogen intermediates to a high level of dynamic equilibrium.

Density functional theory (DFT) calculations were further performed to investigate the  $\text{eNO}_3^-$ RR mechanism and understand the synergistic catalytic behavior of Pd and Ru in  $\text{Pd}_{74}\text{Ru}_{26}$ . Three stable and confirmed surfaces, including Pd(111), Ru(001) and  $\text{Pd}_{74}\text{Ru}_{26}(111)$ , were selected to build models. The adsorption configurations of each intermediate on the three surfaces during the HER and  $\text{eNO}_3^-$ RR steps were optimized (ESI Fig. S29†). Based on the experimental results, the three catalysts all have  $\text{eNO}_3^-$ RR activity and undergo  $\text{NH}_3$ -producing pathways, meaning that they can all reduce  $\text{NO}_3^-$ . However,  $\text{NO}_3^-$  typically has low binding affinity and nucleophilicity on transition metals owing to its symmetrical ( $D_{3h}$ ) resonant structure.<sup>48</sup> Moreover, it is thermodynamically difficult to adsorb negatively charged free  $\text{NO}_3^-$  on the surface of the negative electrode, especially under a more negative reduction potential. Given the strong hydrogen bonding between  $\text{NO}_3^-$  and  $\text{H}_2\text{O}$  in the aqueous electrolyte,<sup>23</sup> the adsorption of  $\text{NO}_3^-$  on the electrode surface largely depends on the affinity for  $\text{H}_2\text{O}$ . Consequently, appropriately enhanced  $\text{H}_2\text{O}$  adsorption on the  $\text{Pd}_{74}\text{Ru}_{26}(111)$  surface compared to Pd(111) and Ru(001) surfaces favors the transport and subsequent reduction of  $\text{NO}_3^-$  (Fig. 5d). This also corresponds to  $\text{Pd}_{74}\text{Ru}_{26}$  exhibiting the most positive onset potential for  $\text{eNO}_3^-$ RR (Fig. 4a). The step from  $^*\text{H}$  to  $\text{H}_2$  on the three surfaces is thermodynamically uphill and the energy barriers are almost identical, which suggests that they all have similar  $^*\text{H}$  retention capabilities. In this case, the  $^*\text{H}$  on the surface of  $\text{Pd}_{74}\text{Ru}_{26}$  will more readily bind to the high-density  $^*\text{NO}_3^-$ , thus facilitating the subsequent proton-coupled electron transfer process to produce  $\text{NH}_3$ .

The most thermodynamically favorable  $\text{eNO}_3^-$ RR pathway on the three surfaces was studied, involving a sequential deoxidation ( $^*\text{NO}_3$  to  $^*\text{N}$ ) followed by a sequential hydrogenation ( $^*\text{N}$  to  $^*\text{NH}_3$ ) process (ESI Fig. S30–S32† and DFT calculations).<sup>17,49,50</sup> The diagram based on the Gibbs free energy change ( $\Delta G$ ) of each reaction state calculated under 0 V is shown in Fig. 5e. In terms of the  $\Delta G$  over the entire  $\text{eNO}_3^-$ RR path, the introduction of Ru into Pd mainly optimizes the deoxidation steps compared to the single components. It can be seen that

the three surfaces all display energy barriers for the protonation of  $^*\text{NO}_2$  and  $^*\text{NO}$ . For the Ru(001) surface, the RDS is the reduction of  $^*\text{NO}_2$  to  $^*\text{ONOH}$  with a high  $\Delta G$  of 0.674 eV, while for the Pd(111) surface, the RDS is the reduction of  $^*\text{NO}$  to  $^*\text{NOH}$  with a higher  $\Delta G$  of 0.715 eV. Alloying Pd and Ru to the  $\text{Pd}_{74}\text{Ru}_{26}(111)$  surface results in the same RDS as for Pd, but with a much lower  $\Delta G$  of 0.47 eV. This is consistent with the experimental results on the order of performance of the catalysts for  $\text{NH}_3$  production *via*  $\text{eNO}_3^-$ RR, *i.e.*,  $\text{Pd}_{74}\text{Ru}_{26} > \text{Ru} > \text{Pd}$ . Appearance of considerable  $\text{NO}_2^-$  FE on Pd may be due to its relatively high  $\Delta G$  of  $^*\text{ONOH}$  as shown in Fig. 5d, which allows the desorption of  $^*\text{ONOH}$  to form  $\text{NO}_2^-$ .

Based on the above analysis, the electronic interactions between Pd and Ru in  $\text{Pd}_{74}\text{Ru}_{26}$  optimize the performance of  $\text{eNO}_3^-$ RR to  $\text{NH}_3$  mainly in two aspects: (1) improving the transport of  $\text{NO}_3^-$  to the catalyst surface by increasing the affinity of  $\text{H}_2\text{O}$ , and (2) lowering the protonation energy barriers for two key intermediates  $^*\text{NO}_2$  (compared to Ru) and  $^*\text{NO}$  (compared to Pd).

### 3. Conclusions

To summarize, we designed a  $\text{Pd}_{74}\text{Ru}_{26}$  bimetallic electrocatalyst *via* a tailored electrodeposition method for highly efficient  $\text{NH}_3$  production *via*  $\text{eNO}_3^-$ RR under alkaline conditions. When operating at the  $\text{NO}_3^-$  concentration (32.3 mM) of typical industrial wastewater,  $\text{Pd}_{74}\text{Ru}_{26}$  exhibits nearly full  $\text{NH}_3$  FE over a wide potential window from 0.1 to  $-0.3$  V, with an average  $\text{NH}_3$  yield rate of  $16.20 \text{ mg h}^{-1} \text{ cm}^{-2}$  at  $-0.3$  V. The potential window for obtaining  $\sim 100\%$   $\text{NH}_3$  FE can be extended from 0.1 to  $-0.9$  V at a  $\text{NO}_3^-$  concentration of 100 mM, with the average  $\text{NH}_3$  yield rate reaching  $42.98 \text{ mg h}^{-1} \text{ cm}^{-2}$  at  $-0.9$  V. Meanwhile,  $\text{Pd}_{74}\text{Ru}_{26}$  also demonstrates excellent electrocatalytic stability during a 114 h CP test. Experimental investigations and DFT calculations suggest that the remarkable performance of  $\text{eNO}_3^-$ RR to  $\text{NH}_3$  originates from the optimized transport of  $\text{NO}_3^-$  and protonation of key intermediates  $^*\text{NO}_2$  (compared to Ru) and  $^*\text{NO}$  (compared to Pd), which benefits from the electronic structure modulation of Pd and Ru in  $\text{Pd}_{74}\text{Ru}_{26}$ . This work provides not only an  $\text{eNO}_3^-$ RR catalyst for  $\text{NH}_3$  production with nearly full FE, but also an effective route to design  $\text{eNO}_3^-$ RR catalysts capable of balancing the adsorption and coupling of  $^*\text{H}$  with various nitrogen intermediates.

### Author contributions

Yue Hu mainly conducted the design, synthesis, structural analysis and electrocatalytic measurements, and prepared the original manuscript. Jiawei Liu, Wenyu Luo, Jinfeng Dong, Carmen Lee, and Hu Erhai assisted with the characterization analysis and electrocatalytic measurements. Zhang Nan assisted with the Operando Fourier transform infrared spectroscopy (FTIR) tests. Mengxin Chen assisted with the  $^1\text{H}$  nuclear magnetic resonance (NMR) testing. Yifan Xu and Dongshuang Wu assisted with the X-ray absorption spectroscopy tests and analysis. Mingsheng Zhang and Qiang Zhu assisted with the X-ray photoelectron spectroscopy tests. Lixiang Zhong assisted



with the density functional theory calculations and analysis. Dongsheng Geng and Qingyu Yan supervised the work and revised the manuscript. All authors participated in the discussion of the results.

## Conflicts of interest

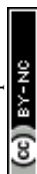
The authors declare no conflicting interests regarding the content of this article.

## Acknowledgements

The authors acknowledge funding support from the 111 Project (no. B170003), Outstanding Young Talents Program (Overseas), Nanjing University of Information Science & Technology, Singapore MOE AcRF Tier 1 grant no. 2020-T1-001-031 and RT6/22, and Singapore RIE2025 USS LCER PHASE 2 PROGRAMME U2305D4001. The XAFS measurement was conducted at BL14b2, SPring-8 under beam proposal 2023A1735. Yifan Xu and Dongshuang Wu acknowledge the NAP-SUG from NTU and tier 1 grant (RG81/22) from MOE to support the overseas XAFS experiments. They also greatly appreciate the technical support from the beam scientists Okkyun SEO and Takeshi WATANABE.

## References

- 1 Y. Wang, C. Wang, M. Li, Y. Yu and B. Zhang, Nitrate electroreduction: mechanism insight, *in situ* characterization, performance evaluation, and challenges, *Chem. Soc. Rev.*, 2021, **50**, 6720–6733.
- 2 A. Valera-Medina, H. Xiao, M. Owen-Jones, W. I. F. David and P. J. Bowen, Ammonia for power, *Prog. Energy Combust. Sci.*, 2018, **69**, 63–102.
- 3 C. Smith, A. K. Hill and L. Torrente-Murciano, Current and future role of Haber–Bosch ammonia in a carbon-free energy landscape, *Energy Environ. Sci.*, 2020, **13**, 331–344.
- 4 J. Lim, C. A. Fernández, S. W. Lee and M. C. Hatzell, Ammonia and nitric acid demands for fertilizer use in 2050, *ACS Energy Lett.*, 2021, **6**, 3676–3685.
- 5 X. Liu, A. Elgowainy and M. Wang, Life cycle energy use and greenhouse gas emissions of ammonia production from renewable resources and industrial by-products, *Green Chem.*, 2020, **22**, 5751–5761.
- 6 J. G. Chen, R. M. Crooks, L. C. Seefeldt, K. L. Bren, R. M. Bullock, M. Y. Darensbourg, P. L. Holland, B. Hoffman, M. J. Janik, A. K. Jones, M. G. Kanatzidis, P. King, K. M. Lancaster, S. V. Lyman, P. Pfromm, W. F. Schneider and R. R. Schrock, Beyond fossil fuel-driven nitrogen transformations, *Science*, 2018, **360**, eaar6611.
- 7 B. H. R. Suryanto, H.-L. Du, D. Wang, J. Chen, A. N. Simonov and D. R. MacFarlane, Challenges and prospects in the catalysis of electroreduction of nitrogen to ammonia, *Nat. Catal.*, 2019, **2**, 290–296.
- 8 I. E. Khalil, C. Xue, W. Liu, X. Li, Y. Shen, S. Li, W. Zhang and F. Huo, The role of defects in metal–organic frameworks for nitrogen reduction reaction: when defects switch to features, *Adv. Funct. Mater.*, 2021, **31**, 2010052.
- 9 C. Lv, J. Liu, C. Lee, Q. Zhu, J. Xu, H. Pan, C. Xue and Q. Yan, Emerging p-block-element-based electrocatalysts for sustainable nitrogen conversion, *ACS Nano*, 2022, **16**, 15512–15527.
- 10 X. Yang, S. Mukherjee, T. O'Carroll, Y. Hou, M. R. Singh, J. A. Gauthier and G. Wu, Achievements, challenges, and perspectives on nitrogen electrochemistry for carbon-neutral energy technologies, *Angew. Chem., Int. Ed.*, 2023, **62**, e202215938.
- 11 D. Liu, L. Qiao, S. Peng, H. Bai, C. Liu, W. F. Ip, K. H. Lo, H. Liu, K. W. Ng, S. Wang, X. Yang and H. Pan, Recent advances in electrocatalysts for efficient nitrate reduction to ammonia, *Adv. Funct. Mater.*, 2023, **33**, 2303480.
- 12 J. Liang, Z. Li, L. Zhang, X. He, Y. Luo, D. Zheng, Y. Wang, T. Li, H. Yan, B. Ying, S. Sun, Q. Liu, M. S. Hamdy, B. Tang and X. Sun, Advances in ammonia electrosynthesis from ambient nitrate/nitrite reduction, *Chem*, 2023, **9**, 1768–1827.
- 13 Z. W. Seh, J. Kibsgaard, C. F. Dickens, I. Chorkendorff, J. K. Nørskov and T. F. Jaramillo, Combining theory and experiment in electrocatalysis: insights into materials design, *Science*, 2017, **355**, eaad4998.
- 14 X. Cui, C. Tang and Q. Zhang, A review of electrocatalytic reduction of dinitrogen to ammonia under ambient conditions, *Adv. Energy Mater.*, 2018, **8**, 1800369.
- 15 H. Shen, C. Choi, J. Masa, X. Li, J. Qiu, Y. Jung and Z. Sun, Electrochemical ammonia synthesis: mechanistic understanding and catalyst design, *Chem*, 2021, **7**, 1708–1754.
- 16 G. Soloveichik, M. Acharya, H. Cheeseman, D. Wicks and D. J. U. D. Tew, *Renewable Energy to Fuels through Utilization of Energy-Dense Liquids (REFUEL)*, US DOE, 2016.
- 17 Y. Wang, A. Xu, Z. Wang, L. Huang, J. Li, F. Li, J. Wicks, M. Luo, D.-H. Nam, C.-S. Tan, Y. Ding, J. Wu, Y. Lum, C.-T. Dinh, D. Sinton, G. Zheng and E. H. Sargent, Enhanced nitrate-to-ammonia activity on copper–nickel alloys *via* tuning of intermediate adsorption, *J. Am. Chem. Soc.*, 2020, **142**, 5702–5708.
- 18 P. G. Falkowski, T. Fenchel and E. F. Delong, The microbial engines that drive earth's biogeochemical cycles, *Science*, 2008, **320**, 1034–1039.
- 19 A. Menció, J. Mas-Pla, N. Otero, O. Regàs, M. Boy-Roura, R. Puig, J. Bach, C. Domènech, M. Zamorano, D. Brusí and A. Folch, Nitrate pollution of groundwater; all right..., but nothing else?, *Sci. Total Environ.*, 2016, **539**, 241–251.
- 20 P. H. van Langevelde, I. Katsounaros and M. T. M. Koper, Electrocatalytic nitrate reduction for sustainable ammonia production, *Joule*, 2021, **5**, 290–294.
- 21 G.-F. Chen, Y. Yuan, H. Jiang, S.-Y. Ren, L.-X. Ding, L. Ma, T. Wu, J. Lu and H. Wang, Electrochemical reduction of nitrate to ammonia *via* direct eight-electron transfer using a copper–molecular solid catalyst, *Nat. Energy*, 2020, **5**, 605–613.
- 22 Y. Wang, M. Sun, J. Zhou, Y. Xiong, Q. Zhang, C. Ye, X. Wang, P. Lu, T. Feng, F. Hao, F. Liu, J. Wang, Y. Ma, J. Yin, S. Chu, L. Gu, B. Huang and Z. Fan, Atomic coordination environment engineering of bimetallic alloy



- nanostructures for efficient ammonia electrosynthesis from nitrate, *Proc. Natl. Acad. Sci. U. S. A.*, 2023, **120**, e2306461120.
- 23 W. He, J. Zhang, S. Dieckhöfer, S. Varhade, A. C. Brix, A. Lielpetere, S. Seisel, J. R. C. Junqueira and W. Schuhmann, Splicing the active phases of copper/cobalt-based catalysts achieves high-rate tandem electroreduction of nitrate to ammonia, *Nat. Commun.*, 2022, **13**, 1129.
  - 24 F.-Y. Chen, Z.-Y. Wu, S. Gupta, D. J. Rivera, S. V. Lambeets, S. Pecaut, J. Y. T. Kim, P. Zhu, Y. Z. Finfrook, D. M. Meira, G. King, G. Gao, W. Xu, D. A. Cullen, H. Zhou, Y. Han, D. E. Perea, C. L. Muhich and H. Wang, Efficient conversion of low-concentration nitrate sources into ammonia on a Ru-dispersed Cu nanowire electrocatalyst, *Nat. Nanotechnol.*, 2022, **17**, 759–767.
  - 25 M. Xie, S. Tang, Z. Li, M. Wang, Z. Jin, P. Li, X. Zhan, H. Zhou and G. Yu, Intermetallic single-atom alloy In–Pd bimetallic for neutral electrosynthesis of ammonia from nitrate, *J. Am. Chem. Soc.*, 2023, **145**, 13957–13967.
  - 26 L. Wu, J. Feng, L. Zhang, S. Jia, X. Song, Q. Zhu, X. Kang, X. Xing, X. Sun and B. Han, Boosting electrocatalytic nitrate-to-ammonia *via* tuning of n-intermediate adsorption on a Zn–Cu catalyst, *Angew. Chem., Int. Ed.*, 2023, **62**, e202307952.
  - 27 Y. Zhou, R. Duan, H. Li, M. Zhao, C. Ding and C. Li, Boosting electrocatalytic nitrate reduction to ammonia *via* promoting water dissociation, *ACS Catal.*, 2023, **13**, 10846–10854.
  - 28 J. Zhou, M. Wen, R. Huang, Q. Wu, Y. Luo, Y. Tian, G. Wei and Y. Fu, Regulating active hydrogen adsorbed on grain boundary defects of nano-nickel for boosting ammonia electrosynthesis from nitrate, *Energy Environ. Sci.*, 2023, **16**, 2611–2620.
  - 29 A. J. Medford, A. Vojvodic, J. S. Hummelshøj, J. Voss, F. Abild-Pedersen, F. Studt, T. Bligaard, A. Nilsson and J. K. Nørskov, From the sabatier principle to a predictive theory of transition-metal heterogeneous catalysis, *J. Catal.*, 2015, **328**, 36–42.
  - 30 K. Fan, W. Xie, J. Li, Y. Sun, P. Xu, Y. Tang, Z. Li and M. Shao, Active hydrogen boosts electrochemical nitrate reduction to ammonia, *Nat. Commun.*, 2022, **13**, 7958.
  - 31 Y. Wu, L. Wang, T. Bo, Z. Chai, J. K. Gibson and W. Shi, Boosting hydrogen evolution in neutral medium by accelerating water dissociation with Ru clusters loaded on Mo<sub>2</sub>CT<sub>x</sub> MXene, *Adv. Funct. Mater.*, 2023, **33**, 2214375.
  - 32 J. Wang, L. Han, B. Huang, Q. Shao, H. L. Xin and X. Huang, Amorphization activated ruthenium–tellurium nanorods for efficient water splitting, *Nat. Commun.*, 2019, **10**, 5692.
  - 33 L. Deng, F. Hu, M. Ma, S.-C. Huang, Y. Xiong, H.-Y. Chen, L. Li and S. Peng, Electronic modulation caused by interfacial Ni–O–M (M = Ru, Ir, Pd) bonding for accelerating hydrogen evolution kinetics, *Angew. Chem., Int. Ed.*, 2021, **60**, 22276–22282.
  - 34 J. Chen, C. Chen, M. Qin, B. Li, B. Lin, Q. Mao, H. Yang, B. Liu and Y. Wang, Reversible hydrogen spillover in Ru–WO<sub>3–x</sub> enhances hydrogen evolution activity in neutral pH water splitting, *Nat. Commun.*, 2022, **13**, 5382.
  - 35 J. Lim, C.-Y. Liu, J. Park, Y.-H. Liu, T. P. Senftle, S. W. Lee and M. C. Hatzell, Structure sensitivity of Pd facets for enhanced electrochemical nitrate reduction to ammonia, *ACS Catal.*, 2021, **11**, 7568–7577.
  - 36 W. Gao, K. Xie, J. Xie, X. Wang, H. Zhang, S. Chen, H. Wang, Z. Li and C. Li, Alloying of Cu with Ru enabling the relay catalysis for reduction of nitrate to ammonia, *Adv. Mater.*, 2023, **35**, 2202952.
  - 37 J.-Y. Fang, Q.-Z. Zheng, Y.-Y. Lou, K.-M. Zhao, S.-N. Hu, G. Li, O. Akdim, X.-Y. Huang and S.-G. Sun, Ampere-level current density ammonia electrochemical synthesis using CuCo nanosheets simulating nitrite reductase bifunctional nature, *Nat. Commun.*, 2022, **13**, 7899.
  - 38 C. Cui, L. Gan, M. Heggen, S. Rudi and P. Strasser, Compositional segregation in shaped Pt alloy nanoparticles and their structural behaviour during electrocatalysis, *Nat. Mater.*, 2013, **12**, 765–771.
  - 39 L. Fan, H. Shen, D. Ji, Y. Xing, L. Tao, Q. Sun and S. Guo, Biaxially compressive strain in Ni/Ru core/shell nanoplates boosts Li–CO<sub>2</sub> batteries, *Adv. Mater.*, 2022, **34**, 2204134.
  - 40 A. J. Bard, L. R. Faulkner and H. S. White, *Electrochemical Methods: Fundamentals and Applications*, John Wiley & Sons, 2001.
  - 41 M. Zhao, L. Xu, M. Vara, A. O. Elnabawy, K. D. Gilroy, Z. D. Hood, S. Zhou, L. Figueroa-Cosme, M. Chi, M. Mavrikakis and Y. Xia, Synthesis of Ru icosahedral nanocages with a face-centered-cubic structure and evaluation of their catalytic properties, *ACS Catal.*, 2018, **8**, 6948–6960.
  - 42 K. Kusada, H. Kobayashi, R. Ikeda, Y. Kubota, M. Takata, S. Toh, T. Yamamoto, S. Matsumura, N. Sumi, K. Sato, K. Nagaoka and H. Kitagawa, Solid solution alloy nanoparticles of immiscible Pd and Ru elements neighboring on Rh: changeover of the thermodynamic behavior for hydrogen storage and enhanced CO–Oxidizing ability, *J. Am. Chem. Soc.*, 2014, **136**, 1864–1871.
  - 43 Z. Qiu, Y. Li, Y. Gao, Z. Meng, Y. Sun, Y. Bai, N.-T. Suen, H.-C. Chen, Y. Pi and H. Pang, 2D MOF-assisted pyrolysis-displacement-alloying synthesis of high-entropy alloy nanoparticles library for efficient electrocatalytic hydrogen oxidation, *Angew. Chem., Int. Ed.*, 2023, **62**, e202306881.
  - 44 R. Chauhan and V. C. Srivastava, Electrochemical denitrification of highly contaminated actual nitrate wastewater by Ti/RuO<sub>2</sub> anode and iron cathode, *Chem. Eng. J.*, 2020, **386**, 122065.
  - 45 Y. Fernández-Nava, E. Marañón, J. Soons and L. Castrillón, Denitrification of wastewater containing high nitrate and calcium concentrations, *Bioresour. Technol.*, 2008, **99**, 7976–7981.
  - 46 World Health Organization, *Guidelines for Drinking-Water Quality: First Addendum to the Fourth Edition*, World Health Organization, 2017.
  - 47 X. Li, P. Shen, X. Li, D. Ma and K. Chu, Sub-nm RuO<sub>x</sub> clusters on Pd metallene for synergistically enhanced nitrate electroreduction to ammonia, *ACS Nano*, 2023, **17**, 1081–1090.
  - 48 Y. Li, Y. K. Go, H. Ooka, D. He, F. Jin, S. H. Kim and R. Nakamura, Enzyme mimetic active intermediates for



nitrate reduction in neutral aqueous media, *Angew. Chem., Int. Ed.*, 2020, **59**, 9744–9750.

- 49 N. C. Kani, N. H. L. Nguyen, K. Markel, R. R. Bhawnani, B. Shindel, K. Sharma, S. Kim, V. P. Dravid, V. Berry, J. A. Gauthier and M. R. Singh, Electrochemical reduction of nitrates on CoO nanoclusters-functionalized graphene with highest mass activity and nearly 100% selectivity to ammonia, *Adv. Energy Mater.*, 2023, **13**, 2204236.
- 50 J.-X. Liu, D. Richards, N. Singh and B. R. Goldsmith, Activity and selectivity trends in electrocatalytic nitrate reduction on transition metals, *ACS Catal.*, 2019, **9**, 7052–7064.

